doi.org/10.36721/PJPS.2025.38.4.REG.14703.1

Integrated *in vivo* and *in silico* ADMET and metabolomic profiling of basil seed bioactives Methyl eugenol and linalool

Mahpara Gondal[1], Muhammad Sajid Hamid Akash*[1] and Kanwal Rehman[2]
[1]Department of Pharmaceutical Chemistry, Government College University, Faisalabad, Pakistan
[2]Department of Pharmacy, The Women University, Multan, Pakistan

Abstract: Biotransformation pathways critically predict rational drug design by elucidating a compound's absorption, distribution, metabolism, excretion and toxicity (ADMET) profile. This investigation provides a consolidated *in vivo* and *in silico* assessment of methyl eugenol (ME) and linalool (LL). Acute oral toxicity studies in Swiss albino rats revealed no mortality or clinical distress up to 2000 mg/kg. Noncompartmental pharmacokinetic analysis showed both compounds reached maximum plasma concentration at 4 hr (413.20 ng/mL for ME; 248.66 ng/mL for LL) and were largely cleared within 24 hrs. Despite identical T_{max} values, their elimination half-lives differed significantly (30.0 h for ME vs. 117.5 h for LL), leading to greater systemic exposure for LL. Time-resolved LC-MS/MS identified distinct phase I metabolic pathways for each compound, which were corroborated by *in silico* predictions. Molecular docking against α-amylase and acetylcholinesterase, indicated favorable binding energies for both compounds, with ME showing slightly stronger affinity in some instances (e.g., -5.6 vs. -5.0 kcal/mol for α-amylase). However, LL consistently exhibited lower RMSD values, suggesting more specific binding. This integrated empirical-computational approach offers a foundational ADMET profile, guiding future structural modifications to optimize their therapeutic potential.

Keywords: Basil seed bioactives; pharmacokinetics; biotransformation; molecular docking; LC-MS/MS metabolite profiling.

Submitted on 03-06-2025 – Revised on 27-06-2025 – Accepted on 01-07-2025

INTRODUCTION

The bioactive terpenoid linalool (LL) and the phenylpropanoid methyl eugenol are abundant constituents of *Ocimum basilicum* (basil) seeds and undergo extensive biotransformation *in vivo*. Investigating these metabolic pathways is essential for defining their pharmacokinetic profiles-namely ADMET-and for anticipating both therapeutic and adverse outcomes. LL is an acyclic monoterpene alcohol ubiquitously distributed across aromatic plants. Preclinical studies have demonstrated that LL exhibits broad-spectrum bioactivities, including antimicrobial, anti-inflammatory, antineoplastic and antioxidant effects (Nöldner, Germer and Koch 2011). Following oral or dermal administration, LL is rapidly absorbed, undergoes phase I and II biotransformations and is eliminated predominantly via renal excretion. Characterization of its metabolites has provided insight into the molecular basis of its pharmacodynamics and safety profile. Methyl eugenol (ME), a methoxylated derivative of eugenol, constitutes a major component of several essential oils. ME displays significant antioxidant capacity and has shown antiproliferative activity in various cancer cell lines, with emerging evidence for neuroprotective efficacy in Alzheimer's disease models and cerebral ischemia-reperfusion injury (de Oliveira *et al.,* 2024).

Conversely, chronic ME exposure has been associated with hepatotoxicity, genotoxicity and perturbations of the gut microbiome, underscoring a narrow therapeutic index and the imperative for rigorous pharmacokinetic and toxicological evaluation. While phase I/II biotransformations often yield metabolites that retain or even enhance therapeutic action, a substantial fraction of xenobiotics are converted into reactive intermediates that elicit adverse effects-ranging from acute organ toxicity to carcinogenesis or other irreversible pathologies. Hepatocytes serve as the principal site for these metabolic reactions, leveraging a complement of CYP450 enzymes, transferases and transporters to mediate both detoxification and bioactivation processes (Ma *et al.,* 2020). A comprehensive, mechanism-based assessment of basil-derived bioactives will therefore require integrated ADMET studies to balance efficacy with safety.

To complement empirical ADMET investigations, *in silico* approaches-chiefly molecular docking and the BioTransformer 3.0 prediction engine-offer mechanistic insight into ligand-receptor interactions and metabolic fate. Molecular docking simulates and ranks binding affinities between candidate ligands (e.g., LL, ME) and putative macromolecular targets implicated in disease, providing estimates of interaction energies and preferred binding conformations (Munir, Akash and Rehman 2025). Concurrently, BioTransformer 3.0 employs rule- and machine learning-based modules to forecast phase I and phase II metabolites, enabling early identification of

**Corresponding author:* e-mail: sajidakash@gcuf.edu.pk

potentially active or toxic biotransformation products (Wishart *et al.,* 2022; Djoumbou-Feunang *et al.,* 2019; Wani *et al.,* 2020). These computational predictions guide experimental prioritization, streamline compound optimization and help anticipate safety liabilities prior to extensive *in vivo* studies. It has been reported that a rhinacanthins-rich *R. nasutus* extract significantly lowered blood glucose and lipid levels in nicotinamide-streptozotocin-induced diabetic rats, supporting the validity of in vivo metabolomic profiling (Shah *et al*., 2019). Furthermore, the extract demonstrated strong superoxide scavenging and antiglycation activities, highlighting the advantage of integrating biochemical assays with metabolomic and in silico analyses for comprehensive phytochemical characterization (Shah *et al*., 2017).

In this study, we generated a comprehensive *in vivo* and *in silico* ADMET profile of basil-derived monoterpenoids ME and LL. Using a rodent model, we first confirmed a favorable acute oral safety margin-evaluating hepatocellular injury markers and gut-microbiota perturbations-then characterized plasma pharmacokinetics (C_{max}, T_{max}, $t_{½}$, AUC) via UV-Vis spectroscopy and high-resolution LC-MS/MS. Sequential phase I and II biotransformations were structurally elucidated, revealing CYP-mediated O-demethylation, hydroxylation, dealkylation and conjugation pathways for both compounds. Complementary BioTransformer 3.0 predictions and molecular docking against inflammatory, neuroprotective and metabolic enzyme targets provided binding-affinity and interaction-profile data.

MATERIALS AND METHODS

Pharmacokinetic and biotransformation analyses were carried out using high-purity LL (≥ 95 % purity; Sigma-Aldrich) and ME (≥ 98 % purity; Macklin). Chromatographic separations and metabolite extractions employed HPLC-grade acetonitrile (Merck) and methanol (Sigma-Aldrich). Analytical-grade sulfuric acid and carbon tetrachloride (Merck and Sigma-Aldrich, respectively) were used in sample processing steps, while a 0.1 M sodium phosphate buffer (pH 7.4; Merck) provided the aqueous medium for biological sample stabilization. Prior to use, all solvents were degassed and filtered through 0.22 µm membranes to ensure reproducibility and optimal performance in both UV-Vis spectrophotometry and LC-MS/MS assays.

Estimation of oral acute toxicity

Oral acute toxicity was assessed in accordance with the OECD 423 guideline using female Swiss albino rats. In brief, animals were assigned to small cohorts and administered a single dose of the test compound by oral gavage. Following dosing, each cohort was observed continuously for the first four hr and then daily over a 14-day period for clinical signs of toxicity and mortality. Body weights were recorded prior to dosing and at regular intervals throughout the study to monitor changes in growth and general health.

Estimation of methyl eugenol and linalool metabolites by in vivo study

Male Swiss albino rats (150-200 g) were housed under controlled vivarium conditions-with a 12 h light/dark cycle, ambient temperature of 22 ± 2 °C and relative humidity of 50 ± 10 %-and provided with standard chow and water *ad libitum*. Following a one-week acclimatization period, animals were randomized into treatment groups and administered a single oral dose of ME or LL via gavage. Blood and tissue samples were collected at predetermined time points post-dosing for metabolite profiling. All procedures were conducted in compliance with national and institutional guidelines for animal welfare and were approved by the Institutional Review Board of Government College University Faisalabad (GCUF/ERC/594). Investigational compounds were administered as a single oral bolus (10 mL/kg body weight) to anesthetized rats. Blood samples were collected via cardiac puncture at 2, 4, 8, 12 and 24 hr post-dose into heparinized tubes. After clot formation, samples were centrifuged at 3,000 rpm for 20 minutes at 4 °C to isolate serum. The resulting serum fractions were then analyzed by UV-Vis spectrophotometry and LC-MS/MS to identify and quantify parent compounds and their metabolites.

Spectroscopic analysis

Primary stock solutions of LL and ME were prepared by accurately weighing each reference standard and dissolving in methanol to yield a defined concentration. Working calibration standards were then generated by serial dilution of the primary stocks with methanol to obtain final concentrations of 40, 60, 80 and 100 µg/mL. A 0.1 M sodium phosphate buffer (pH 7.0) was prepared in distilled water and adjusted with 0.1 M orthophosphoric acid to maintain physiological pH. Quantitative serum concentrations were analyzed to derive key pharmacokinetic parameters using established noncompartmental methods: the elimination half-life ($t_{½}$) was calculated via $t_{½} = \ln(2)/k_{el}$, where k_{el} is the terminal elimination rate constant; the area under the concentration–time curve (AUC) was determined by the trapezoidal rule; and the apparent volume of distribution (V_d/F) and clearance (CL/F) were computed from standard equations relating dose, AUC and k_{el}.

Metabolomic profiling by LC-MS/MS

Serum metabolomic profiling following LL and ME administration was performed using LC-MS/MS. Whole blood was centrifuged at 3,500 × g for 10 minutes at 4 °C to isolate serum, which was then stored at -80 °C until analysis. Metabolite extraction was accomplished by adding methanol to 10 µL of thawed serum to precipitate proteins (10 minutes incubation at room temperature), followed by centrifugation at 16,000 × g for 15 minutes to

remove the precipitate. The resulting supernatant was dried under a gentle stream of nitrogen and the residue reconstituted in 20 µL of methanol. A 10 µL aliquot of this solution was injected for LC-MS/MS analysis, enabling sensitive, high-throughput detection and quantification of endogenous and xenobiotic-derived metabolites (Hadi *et al.,* 2017).

Instrument specifications

Serum concentrations of LL and ME were quantified using an Agilent 1260 Infinity II UHPLC system coupled to an Agilent 6470 triple-quadrupole mass spectrometer. Chromatographic separation was performed on an Agilent ZORBAX Eclipse Plus C18 rapid-resolution HD column (2.1 mm × 50 mm, 1.8 µm particle size) maintained at 30 °C. A binary gradient elution-delivered at a flow rate of 0.5 mL/min-enabled efficient resolution of parent compounds and their metabolites. Mass spectrometric detection utilized electrospray ionization in positive mode (ESI^+) with optimized source and gas parameters to maximize sensitivity. Detailed operating conditions, including gradient composition, ion source settings and MRM transitions, are summarized in table 1.

Metabolomic data acquisition and quantification via LC-MS/MS

Metabolomic profiling was performed using ESI^+ at a capillary voltage of 4.0 kV. Full-scan MS^1 spectra were acquired over an m/z range of 50-400, with data-dependent acquisition triggering MS/MS fragmentation by collision-induced dissociation (CID) at 10-23 eV for selected precursor ions. Metabolite identification and structural confirmation were achieved by matching accurate precursor *m/z* values and diagnostic production spectra to authentic reference standards, in-house and public spectral libraries (e.g., BioTransformer 3.0) and published fragmentation patterns. Quantification of LL, ME and their metabolites employed an external calibration strategy. A 100 ng/mL working standard in acetonitrile was serially diluted and spiked into blank plasma to generate thirteen calibration levels (0.005-250 ng/mL). Peak areas of analyte ions were plotted against nominal concentrations and fitted by linear regression to construct calibration curves. Rat plasma samples collected at 4, 8, 12 and 24 hr post-dose were processed identically-undergoing protein precipitation, centrifugation and supernatant recovery-prior to injection. Sample peak areas were then interpolated against the calibration models to determine absolute concentrations at each time point (Makhdoom *et al.,* 2024).

Computational analysis

In Silico metabolite prediction by biotransformer 3.0

BioTransformer 3.0 (https://biotransformer.ca/new) is an open-access, dual-mode computational platform-accessible via web portal and command-line interface-designed for rapid, reliable prediction and identification of xenobiotic biotransformations. Its architecture comprises two core modules: the Metabolism Prediction Tool (BMPT), which forecasts phase I and II metabolic reactions and the Metabolite Identification Tool (BMIT), which matches experimental spectral data to candidate metabolites. Metabolite prediction combines machine learning algorithms with a curated, knowledge-based rule engine. Structures of parent compounds were drawn in ChemDraw and exported as SMILES strings, which were uploaded to the BioTransformer interface. Within seconds, the platform generated a comprehensive list of putative metabolites for downstream analysis (Terfloth, Bienfait and Gasteiger 2007).

Molecular docking and active site analysis

Active-site residues for LL and ME metabolites were identified through a combination of literature review and *in silico* pocket-detection tools, including the Computed Atlas of Surface Topography of Proteins (CASTp) and PUResNetV2.0. Key catalytic or binding–site residues were mapped as HIS 314 in α-amylase, TYR 136 in acetylcholinesterase, CYS 244 in lipase, THR 337 in β-glucosidase and GLU 67 in serine protease. Subsequent molecular docking simulations were performed using PyRx version 3 and SwissDock to evaluate the binding affinities and preferred orientations of each metabolite within these defined pockets (El-Sonbati *et al.,* 2021). Resulting protein–ligand complexes were visualized in BIOVIA Discovery Studio and PyMOL to characterize hydrogen bonds, hydrophobic contacts and other noncovalent interactions underpinning potential bioactivity.

STATISTICAL ANALYSIS

All pharmacokinetic parameters were analyzed using GraphPad Prism version 10.0. Data are presented as mean ± standard deviation (SD). Descriptive statistics were used to characterize concentration–time profiles, with noncompartmental methods applied to derive key metrics (T_{max}, C_{max}, AUC, $t_{½}$). Between-group comparisons of linalool and methyl eugenol parameters were conducted using unpaired Student's t-tests or one-way ANOVA followed by Tukey's post hoc test, as appropriate. Normality of residuals and homogeneity of variances were verified prior to inferential testing. Linear and nonlinear regression analyses were performed to model concentration-time data, with goodness-of-fit assessed by R^2 values. Statistical significance was defined as $p < 0.05$.

RESULTS

Analysis of oral acute toxicity

Oral acute toxicity of LL and ME was evaluated in male Swiss albino rats according to OECD Guideline 423. Single doses up to 2000 mg/kg body weight were administered by gavage and animals were monitored continuously for the first four hr and then daily for 14 days.

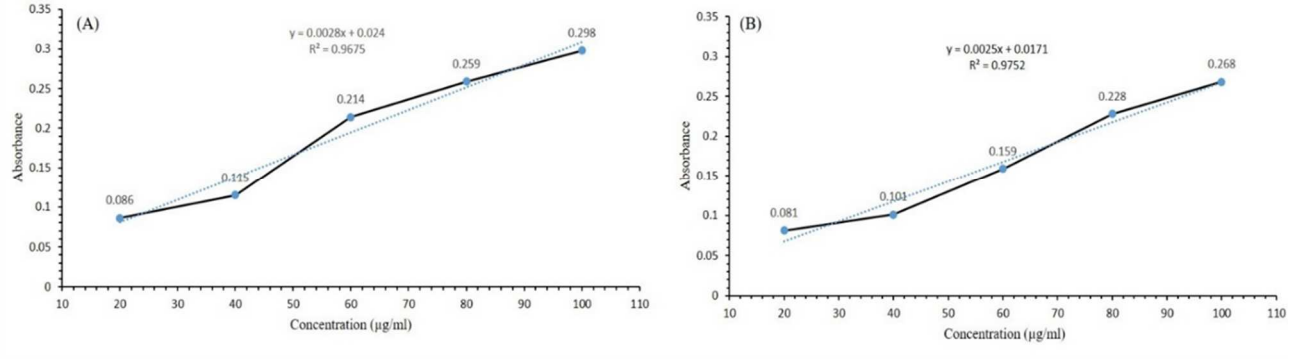

Fig. 1: Calibration curves for Methyl Eugenol and Linalool.

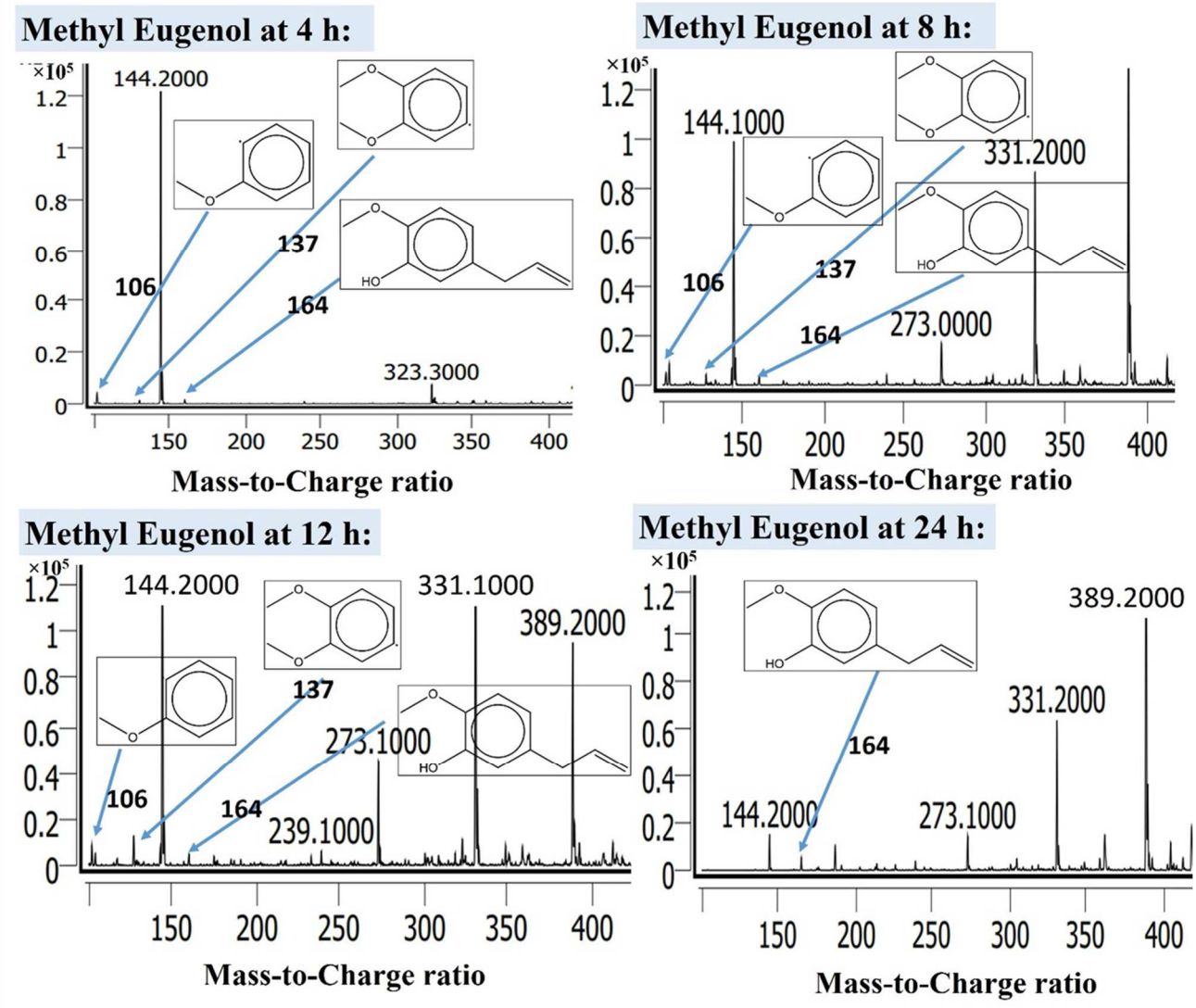

Fig. 2: Temporal Mass Spectrometric Profiling of Methyl Eugenol Biotransformation.

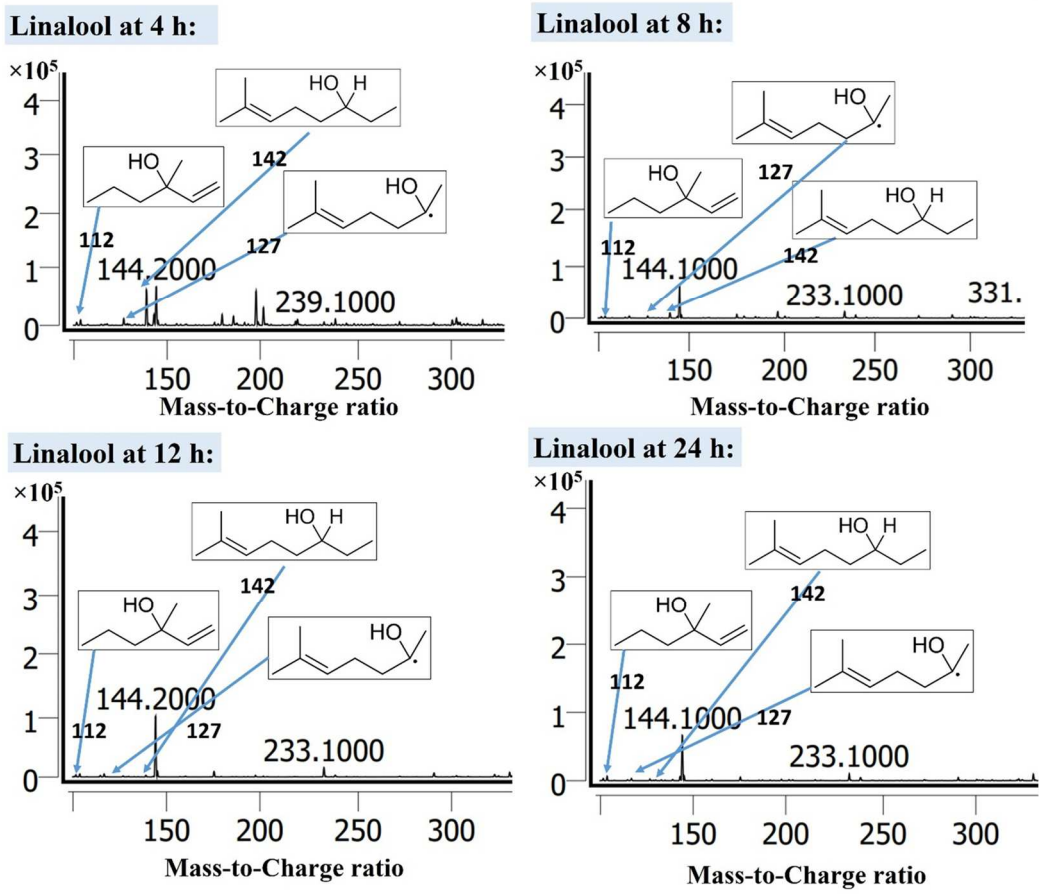

Fig. 3: Temporal Mass Spectrometric Profiling of Linalool Biotransformation.

Table 1: Optimized LC-MS/MS Operating Conditions for the Quantification of Methyl Eugenol and Linalool.

LC-MS/MS operating parameters					
UHPLC Parameters	Value				
Injection volume (µL)	10				
Mobile phase A	0.1% Formic acid in water				
Mobile phase B	0.1% Formic acid in acetonitrile				
Gradient Elution Mode	0.00 min	70% B			
	1.50 min	95% B			
	2.60 min	70% B			
MS/MS Parameters	Value (+)				
Ionization	Air Jet Stream (AJS) Electron Spray Ionization (ESI)				
Polarity	Positive				
Gas Temperature (°C)	300				
Sheath Gas Temperature (°C)	325				
Nitrogen Gas Flow (L/min)	10				
Nebulizer Pressure (psi)	40				
Capillary voltage (V)	4000				
Nozzle voltage/ Charging (V)	1500				
MRM Transitions Used					
Compound	Precursor ion	Product ion	Dwell time (ms)	Fragmentor voltage (V)	Collision Energy (V)
Methyl Eugenol	177.1	134 104	100	135	23
Linalool	155.2	137.1 81.1		115	10 20

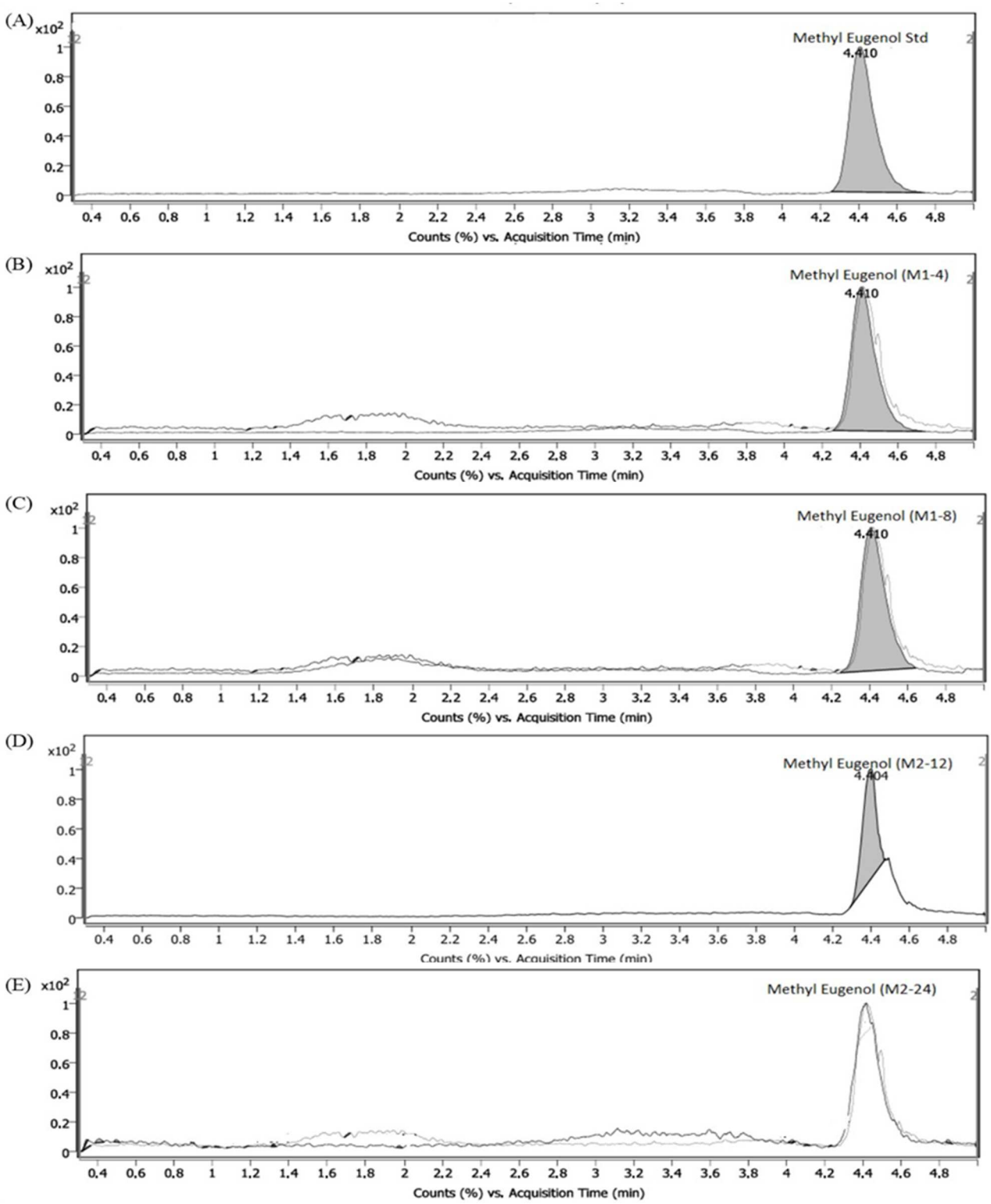

Fig. 4: Time-Dependent LC-MS/MS Quantification of Methyl Eugenol.

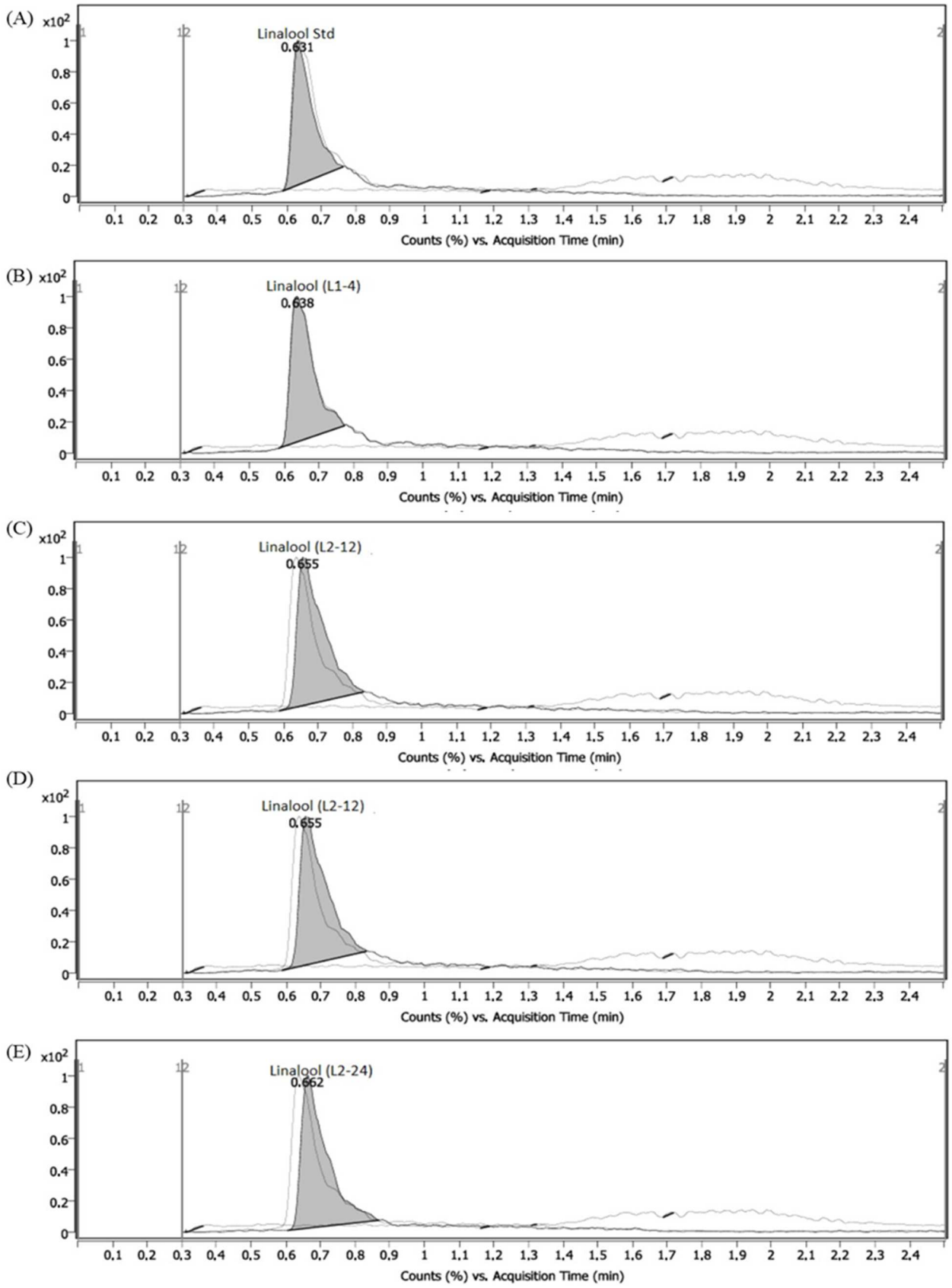

Fig. 5: Time-Dependent LC-MS/MS Quantification of linalool.

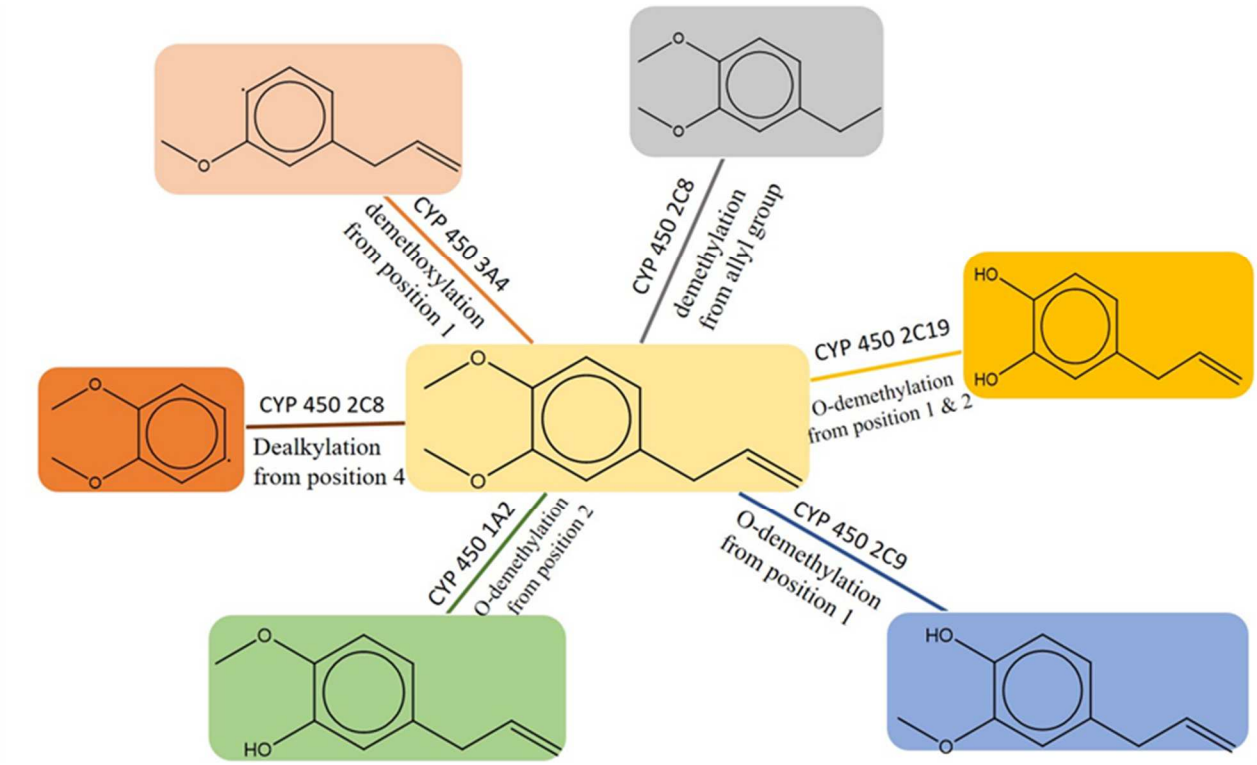

Fig. 6: Prediction of Methyl Eugenol Metabolic Fate: Role of CYP450 Enzymes and Associated Biotransformation Pathways.

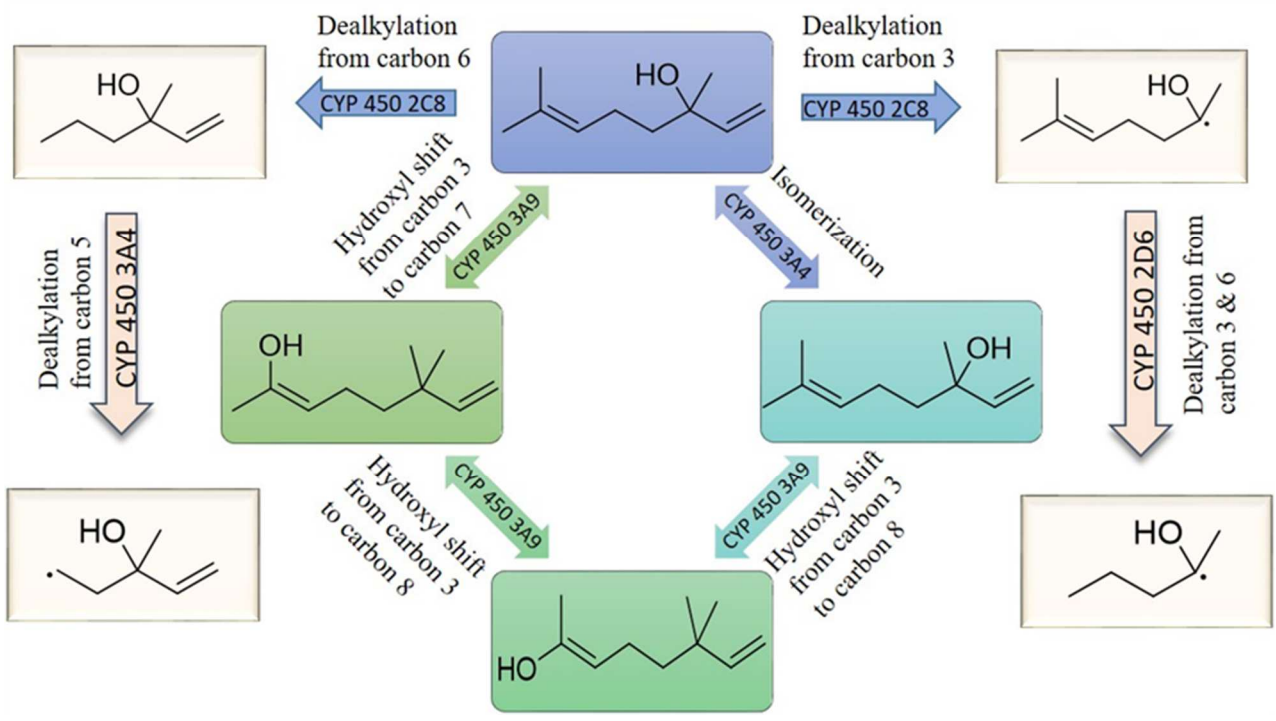

Fig. 7: Predicting the Metabolic Fate of Linalool: Role of Cytochrome P450 Enzymes and Biotransformation Pathways.

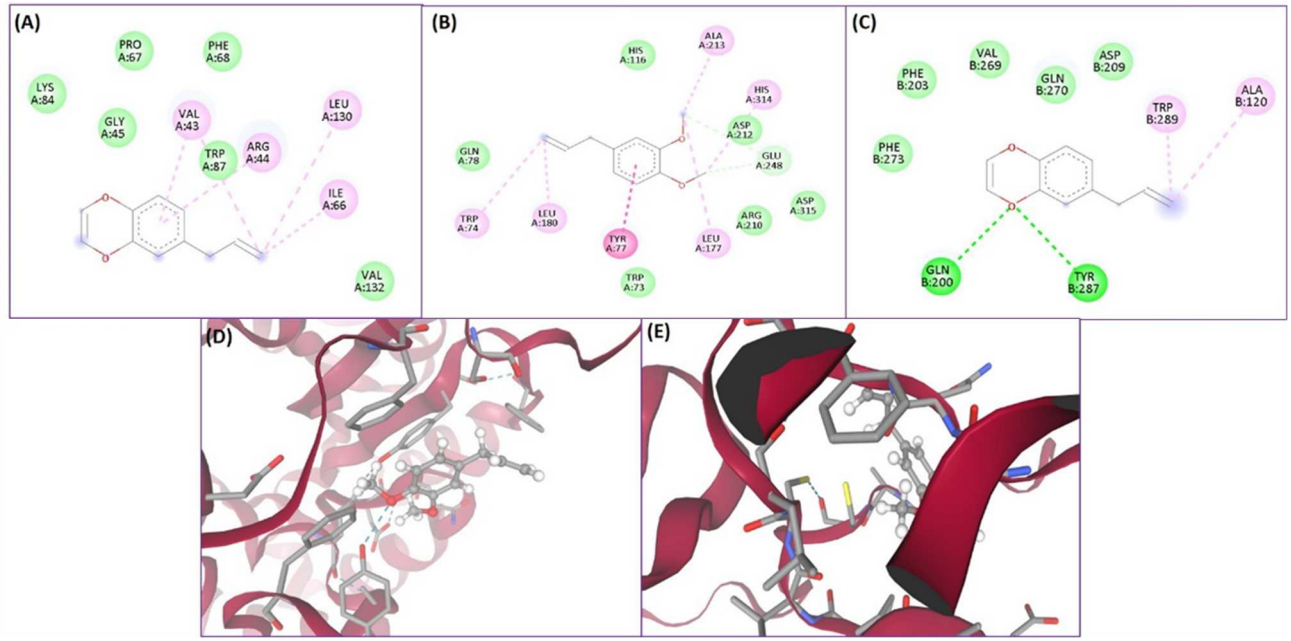

Fig. 8: Predicted binding modes and interactions of the methyl eugenol metabolite with α-amylase (A), acetylcholinesterase (B), lipase (C), β-glucosidase (D), and serine protease (E).

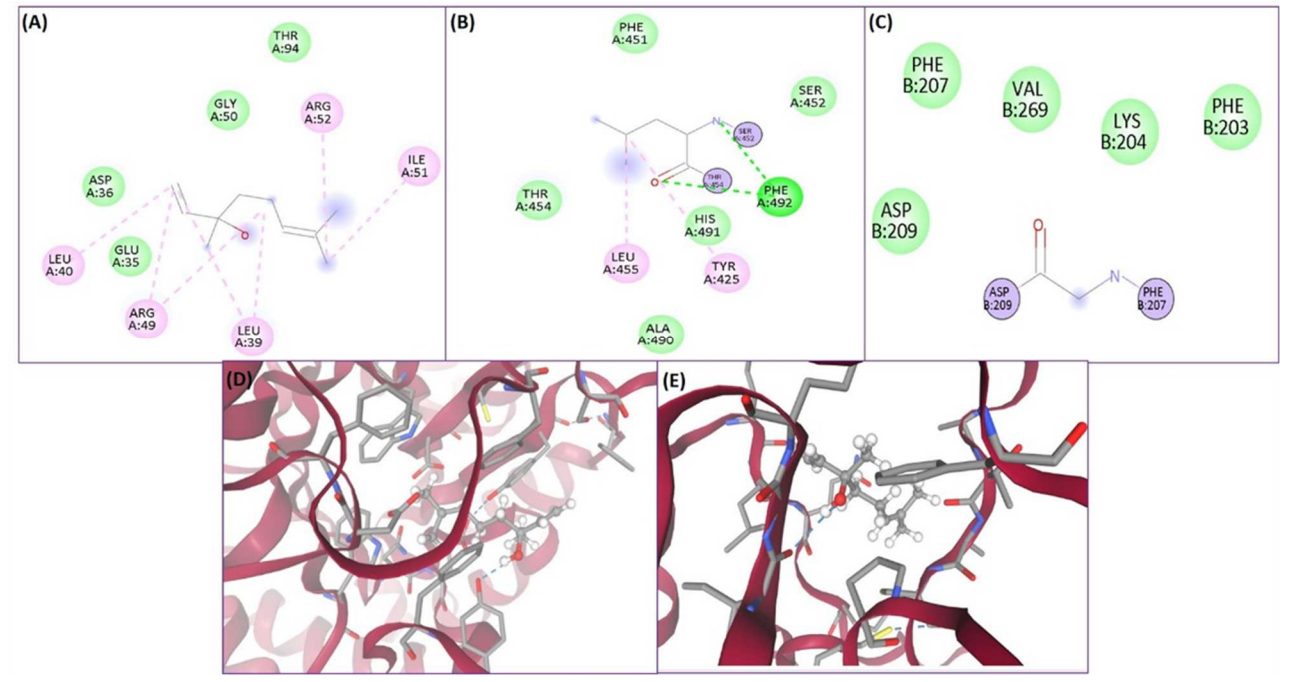

Fig. 9: Predicted binding modes and interactions of linalool metabolite with α-Amylase (A), Acetylcholinesterase (B), Lipase (C), β-Glucosidase (D), and Serine protease (E).

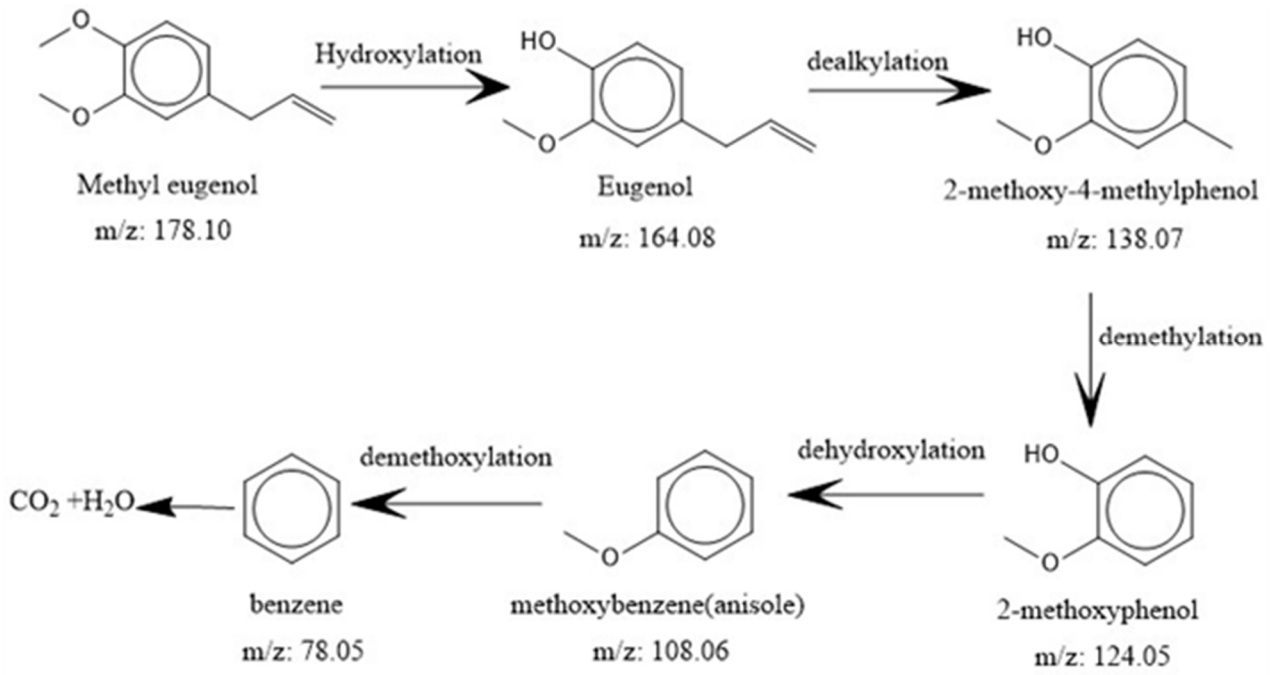

Fig. 10: Proposed metabolic pathway of methyl eugenol.

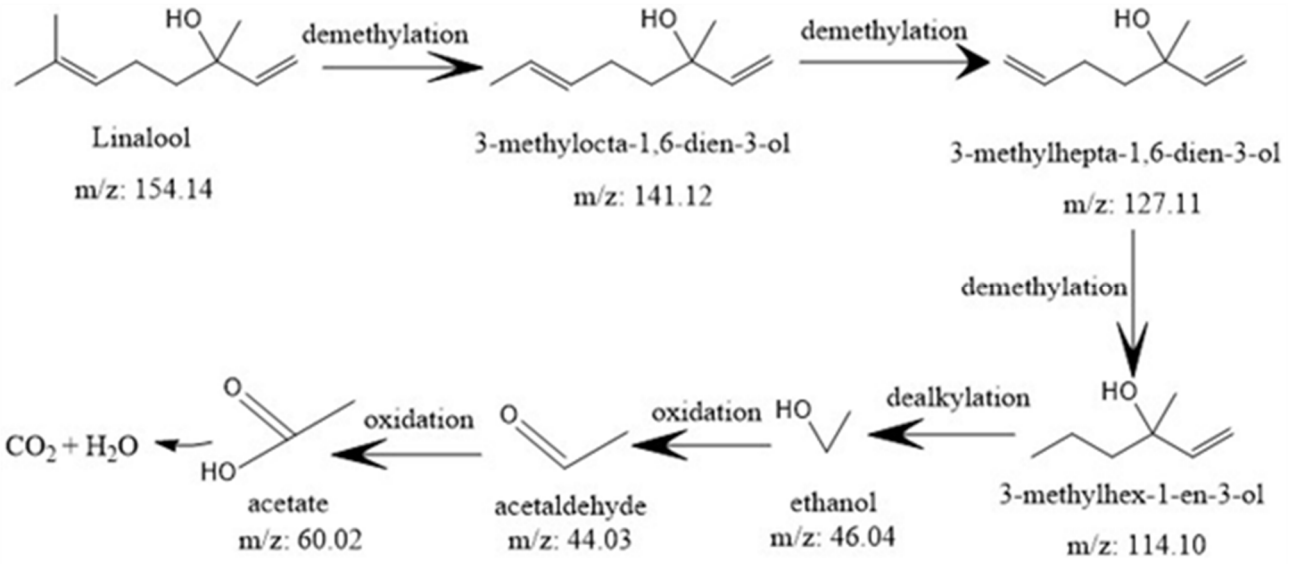

Fig. 11: Proposed metabolic pathway of linalool.

Table 2: Pharmacokinetic Parameters for Methyl eugenol and Linalool.

Pharmacokinetic parameters	Methyl eugenol	Linalool
C_{max}	0.199 ng/ml	0.186 ng/ml
T_{max} (h)	4 h	4 h
Average half-life (h)	30.0 h	117.46 h
Elimination rate constant	0.0231 /h	0.0059/h
AUC (0-24h)	156.88	654.62
Bioavailability (%)	61.4%	58.57%
Clearance	1.35ml/h/kg	1.18ml/h/kg
Volume of distribution (V_d)	14.55ml/kg	17.34ml/kg
Mean residence time (MRT)	42.53 h	171.05 h

Table 3: Summary of Significant Metabolites and Fragments from Spectrums obtained through LC-MS/MS and Predicted Biotransformation of Methyl eugenol and Linalool.

Compound	m/z	Identification	Key Time Points	Hypothesized Origin
Linalool	112	Linalool Oxide	Prominent at 4h; Detected consistently at 8h, 12h & 24h	Dealkylation (CYP-mediated)
	127	Oxidized Acyclic Linalool Fragment	Base peak at 4h; ↓ by 8h & 12h; ↓↓ by 24h	CYP2C8-mediated Dealkylation
	142	8-Hydroxylinalool fragment	Prominent at 4h; ↓ by 8h & 12h; ↓↓ by 24h	Biotransformation
	102	Linalool Oxide fragment	Base peak at 4h; ↓ by 8h & 12h; ↓↓ by 24h	Metabolic cleavage
Methyl eugenol	106	Methoxybenzylium Ion Fragment	Low at 4h; ↑↑ by 8h & 12h; diminishes at 24h	Demethoxylation & Dealkylation mediated by CYP3A4 & CYP2C8 respectively
	137	1,2-dimethoxybenzene	Base peak at 4h; ↑ by 8h; ↑↑ 12h; diminishes at 24h	Dealkylation mediated by CYP2C8
	144	Characteristic fragment Safrole	Prominent at 4h; ↓ consistently at 8h & 12h; ↓↓ by 24h	Metabolic cleavage
	164	5-allyl-2-methoxyphenol	Detected 4h; ↑ by 8h, & 12h; ↑↑ by 24h	O-demethylation (CYP-mediated 1A2)
	331	1'-Hydroxymethyl Eugenol	prominent peak at 8h; ↑ by 12h; ↓ by 24h	Phase I oxidative metabolic pathway.

Table 4: Pharmacokinetic data for Methyl Eugenol and Linalool in blood samples collected at 4, 8, 12, and 24 hr Post-administration.

Time (hr)	Blood Concentration (ng/mL)		P value
	Methyl Eugenol	Linalool	
4	413.20	248.66	< 0.05
8	10.31	16.20	< 0.05
12	1.58	5.15	< 0.05
24	0.26	0.38	> 0.05

Table 5: Predicted Binding Affinities (kcal/mol) and Root Mean Square Deviations (Å) for Methyl eugenol and Linalool docked to selected enzymes.

Receptors	Binding Affinity		RMSD/upper bound		RMSD/lower bound	
	linalool	Methyl eugenol	Linalool	Methyl eugenol	linalool	Methyl eugenol
α-Amylase	-5.0	-5.6	27.245	16.896	25.488	13.802
Acetyl cholinesterase	-3.7	-4.6	16.793	19.425	15.229	18.719
Lipase	-5.1	-5.2	3.661	23.625	2.525	22.528
β-Glucosidase	-5.4	-5.3	6.125	21.554	5.747	19.421
Serine protease	-5.2	-5.0	12.541	25.136	11.431	21.244

The acute oral toxicity assessment revealed a favorable safety profile for both LL and ME up to the limit dose tested. During the 14-day post-administration period, no lethal or significant toxicological endpoints were reached. All animals manifested normal somatic growth, evidenced by consistent body weight gain and maintained complete integumentary integrity, with no incidence of dermal lesions or alopecia observed throughout the study (Api *et al.,* 2018).

Quantification of methyl eugenol in serum by UV-VIS spectrophotometry

The calibration curve for ME (fig. 1A) was generated using standard solutions ranging from 20 to 110 µg/mL. Absorbance measurements were acquired at the compound's λ_{max} and linear regression analysis yielded an R^2 value indicative of excellent correlation between concentration and absorbance. This robust linearity across the entire concentration range permitted precise

quantification of ME in serum samples collected over the 24-hr post-dose period, thereby ensuring both accuracy and reproducibility in the determination of unknown analyte levels.

Quantification of linalool in serum by UV-VIS spectrophotometry

The calibration curve for LL (fig. 1B) was generated using standard solutions prepared according to the protocol described for methyl eugenol (20-110 µg/mL). Absorbance measurements were recorded at the compound's λ_{max} and linear regression analysis produced an R^2 value indicative of excellent correlation between concentration and absorbance. This high degree of linearity across the entire 24-hr sampling interval enabled accurate and reproducible quantification of LL in serum matrices.

Pharmacokinetic profiling of methyl eugenol and linalool

Pharmacokinetic parameters for methyl eugenol and linalool were derived from serum concentration–time data collected over a 24-hr period. ME reached a C_{max} of 0.199 ng/mL at T_{max} = 4 h. Its Cl/F was 1.35 $mL \cdot h^{-1} \cdot kg^{-1}$ and the $t_{½}$ was 30.0 h. The compound exhibited a systemic bioavailability of 61.4%, an apparent V_d/F of 14.55 mL/kg and a MRT of 9.93 hr.

In contrast, LL displayed a C_{max} of 0.186 ng/mL at T_{max} = 4 h, with an apparent clearance of 1.18 $mL \cdot h^{-1} \cdot kg^{-1}$ and a substantially longer t_½ of 117.46 h. LL's systemic bioavailability was 58.6%, its V_d/F was 17.34 mL/kg and the MRT was 171.05 h. These pharmacokinetic profiles (table 2) provide critical insight into the disposition, efficacy potential and dosing considerations for these basil-derived bioactives.

Analysis of metabolites profiling via LC-MS/MS

Identification of methyl eugenol metabolites

LC-MS/MS analysis provided a time-resolved profile of ME biotransformation, as evidenced by the detection of characteristic fragment ions (fig. 2). Comparative evaluation of mass spectra collected at 4, 8, 12 and 24 hr post-administration revealed substantial variations in the relative intensities of specific diagnostic ions.

Identification of methoxybenzyl ion fragment

The ion detected at *m/z* 106 corresponds to a methoxybenzyl radical cation, likely generated through the cleavage of the allyl side chain followed by demethoxylation of the benzene moiety. This fragment was observed at a relatively low abundance at 4 hr post-administration, exhibited a consistent increase at 8 and 12 hr and then declined markedly, approaching baseline levels by 24 hr.

Identification of 1,2-dimethoxybenzene fragment

The peak observed at *m/z* 137 is identified as 1,2-dimethoxybenzene and appears as the base peak in the 4-hr post-administration spectrum. Its abundance increased significantly at 8 hr, peaked at 12 hr and declined sharply by 24 hr. The formation of this metabolite from ME suggests dealkylation mediated by CYP450 enzyme CYP2C8, resulting in the complete removal of the allyl group from the benzene ring.

Identification of safrole fragment

A prominent ion detected at *m/z* 144.2000 corresponds to safrole, indicating that demethoxylation followed by intramolecular cyclization occurred to form the methylenedioxy bridge. This fragment was most abundant at the 4-hr time point, followed by a consistent decrease at 8 and 12 hr. By 24 hr, its abundance had declined to approximately one-fourth of the level observed at 4 hr.

Identification of 5-Allyl-2-methoxyphenol

The ion at *m/z* 164 corresponds to eugenol (5-allyl-2-methoxyphenol), indicating that O-demethylation-likely mediated by CYP1A2-of ME to its phenolic analogue is an early and significant biotransformation pathway. This fragment was detected at 4 hr with a minimal peak, followed by a persistent increase at 8 and 12 hr and was dominantly amplified by 24 hr.

Identification of 1'-hydroxymethyl eugenol

A highly prominent peak emerges at *m/z* 331.2000 at 8 hr and persists at 12 hr but diminishes by 24 hr. The structure is consistent with 1′-hydroxymethyl eugenol, formed through hydroxylation at the C1′ position (benzylic carbon) of the allyl side chain of methyl eugenol.

Identification of linalool metabolites

LC-MS/MS analysis, as depicted in fig. 3, provided a time-resolved overview of LL biotransformation by monitoring its characteristic fragment ions. A comparative assessment of spectra collected at 4, 8, 12 and 24 hr post-administration revealed significant variations in the relative intensities of key fragment ions.

Identification of linalool oxide fragment

The ion detected at *m/z* 112 corresponds to a linalool oxide derivative. The formation of this moiety from LL suggests a dealkylation reaction mediated by CYP2C8. This fragment was prominently observed at 4 hr and maintained a consistent intensity at 8, 12 and 24 hr, indicating a stable presence of this metabolite throughout the sampling period.

Identification of oxidized acyclic linalool fragment

The fragment observed at *m/z* 127 is characterized as an oxygenated, acyclic C_8 radical cation. This ion likely originates from a hydroxylated linalool intermediate through a CYP-mediated oxidation process. It appears as the base peak in the 4-hr spectrum, with its abundance gradually decreasing at 8 and 12 hr and nearly diminishing by 24 hr.

Identification of 8-hydroxylinalool fragment

The ion at *m/z* 142 corresponds to 8-hydroxylinalool, a Phase I metabolite of LL formed via CYP-catalyzed allylic hydroxylation at the C8 methyl terminus. This fragment appeared prominently in the 4- hr spectrum. Its abundance gradually declined at 8 and 12 hr and was markedly diminished by 24 hr, as presented in table 3.

Identification of linalool oxide fragment

The ion detected at *m/z* 102 corresponds to a linalool oxide fragment. The formation of this moiety from linalool oxide suggests dealkylation mediated by CYP2C9. This fragment was clearly present at 4 hr and maintained a consistent abundance at 8, 12 and 24 hr.

Quantification of linalool and methyl eugenol

The LC-MS/MS analysis revealed the time-dependent stability and degradation profile of ME. The standard ME exhibited a distinct retention time at 4.410 minutes. At the 4-hr and 8-hr time points, ME remained largely stable, as evidenced by comparable peak intensities and sharp peak shapes, indicating minimal degradation. However, by 12 hr, a noticeable reduction in peak intensity was observed, with the retention time slightly shifting to 4.404 minutes and the peak appearing broader. This degradation became more pronounced at the 24-hr time point, where the ME peak further diminished in intensity and displayed significant broadening, indicating extensive biotransformation (fig. 4).

The LC-MS/MS analysis revealed a time-dependent degradation profile of linalool under the experimental conditions. The standard LL exhibited a distinct retention time at 0.631 minutes. At 4 hr post-administration, LL remained largely stable, with a comparable peak intensity and a slightly shifted retention time of 0.638 minutes. A modest reduction in concentration was observed at 8 and 12 hr, with the peak appearing at 0.655 minutes at both time points. By 24 hr, a more pronounced decline in peak intensity was noted, with the retention time further shifting to 0.662 minutes. This progressive reduction and retention time drift indicates significant degradation and metabolic transformation of LL over the 24-hr period (fig. 5).

The pharmacokinetic analysis indicated that both ME and LL reached their C_{max} at 4 hr post-administration, measuring 413.20 ng/mL and 248.66 ng/mL, respectively. Following this peak, both compounds demonstrated a rapid elimination phase. By 8 hr, serum concentrations had markedly decreased to 10.31 ng/mL for ME and 16.20 ng/mL for LL. This declining trend continued, with concentrations falling to minimal levels at 24 hr-0.26 ng/mL for ME and 0.38 ng/mL for LL. These values, presented in table 4, were derived through LC-MS/MS quantification, using integrated peak areas from serum chromatograms and corresponding calibration curves generated from standards of known concentrations.

A statistical analysis of the pharmacokinetic data reveals significantly distinct profiles for ME and LL. Initially, at the 4-hr mark, methyl eugenol demonstrates a substantially and statistically significantly higher peak blood concentration ($p < 0.05$), suggesting more rapid or extensive initial absorption. However, this trend dramatically inverts at the 8 and 12-hr intervals, where linalool maintains a statistically significantly higher concentration ($p < 0.05$), indicating a much slower clearance rate and a longer elimination half-life compared to the rapidly cleared methyl eugenol. By 24 hr, the concentrations of both compounds are minimal and the difference between them becomes statistically insignificant ($p > 0.05$), confirming near-total elimination from systemic circulation for both, although distinctly different temporal pathways.

Computational analysis

In-Silico simulation of biotransformation pathways and computational prediction of metabolites by biotransformer 3

The *in silico* predictions of the metabolic fate of ME and LL, performed using the BioTransformer 3.0 platform, are illustrated in fig. 6 and 7, respectively. For ME, the simulation forecasted multiple CYP450-mediated transformations. Notably, O-demethylation at positions 1 and 2-catalyzed by CYP2C9 and CYP1A2-resulted in the formation of 4-allyl-2-methoxyphenol and 5-allyl-2-methoxybenzene, respectively. Concurrent O-demethylation at both positions, mediated by CYP2C19, yielded 4-allylbenzene-1,2-diol. Additionally, demethylation of the allyl group and complete removal of the allyl side chain from the para-position (position 4) of the benzene ring-predicted to be mediated by CYP2C8-led to the formation of 4-ethyl-1,2-dimethoxybenzene and 1,2-dimethoxybenzene. Another predicted transformation involved O-demethoxylation at position 1 of the benzene ring, mediated by CYP3A4, resulting in the generation of 3-allyl-methoxybenzene (anisole). In contrast, linalool underwent fewer biotransformation events but prominently exhibited structural isomerization. CYP3A4 and CYP3A9 were predicted to catalyze hydroxyl group shifts from carbon positions 3 to 7 and 8, leading to various isomeric forms of linalool. Dealkylation at the C3 and C6 positions-mediated by CYP2C8-resulted in the generation of oxidized acyclic linalool fragments and linalool oxide fragments. These metabolites were further predicted to undergo sequential dealkylation reactions, forming secondary daughter fragments.

Analysis of docking targets and binding affinity

To evaluate the binding affinities of ME and LL metabolites, we selected a panel of pharmacologically relevant protein targets: α-amylase, acetylcholinesterase, lipase, β-glucosidase and serine protease. Acetylcholinesterase, a critical enzyme in cholinergic neurotransmission and a validated target in

neurodegenerative disease therapy, was included to explore the potential modulatory effects of these metabolites on neuronal function. Concurrently, α-amylase, lipase, β-glucosidase and serine protease-key enzymes in carbohydrate, lipid and protein metabolism-were chosen to assess possible interactions of the drug metabolites with fundamental digestive and metabolic pathways.

Table 5 summarizes the molecular docking results, including binding energies and conformational stability-expressed as RMSD lower and upper bounds-for ME and LL against five enzyme targets. Both phytochemicals exhibited generally favorable affinities, with ME showing marginally superior binding energies for α-amylase (-5.6 vs. -5.0 kcal/mol) and acetylcholinesterase (-4.6 vs. -3.7 kcal/mol). In contrast, LL displayed slightly stronger interactions with β-glucosidase (-5.4 vs. -5.3 kcal/mol) and serine protease (-5.2 vs. -5.0 kcal/mol), while affinities for lipase were nearly equivalent (-5.1 vs. -5.2 kcal/mol). RMSD values provided insight into complex stability. Despite similar binding energies for lipase, LL exhibited notably low RMSD bounds (2.525-3.661 Å), indicating a highly stable binding pose. LL also demonstrated lower RMSD ranges for β-glucosidase (5.747-6.125 Å) and serine protease (11.431-12.541 Å) compared to methyl eugenol (19.421-21.554 Å and 21.244-25.136 Å, respectively). Conversely, both ligands showed elevated RMSD values when docked to α-amylase (linalool: 25.488-27.245 Å; methyl eugenol: 13.802-16.896 Å) and acetylcholinesterase (linalool: 15.229-16.793 Å; methyl eugenol: 18.719-19.425 Å), suggesting greater conformational flexibility or multiple binding modes.

Molecular docking interactions of methyl eugenol with enzyme targets

Molecular docking simulations (fig. 8) elucidated the binding modes of ME within the active sites of α-amylase, acetylcholinesterase, lipase, β-glucosidase and serine protease. Across all targets, ME engaged in a network of hydrogen bonds, hydrophobic contacts and π-system interactions. Its oxygenated functionalities (methoxy and methylenedioxy groups) formed hydrogen bonds with polar residues-specifically TYR A77 in acetylcholinesterase and both GLN B200 and TYR B287 in lipase (fig. 8B and 8C, respectively). Concurrently, the aromatic ring and allyl side chain established hydrophobic and π-interactions (e.g., π-alkyl and π–π stacking) with nonpolar/aromatic residues such as TRP A87 in α-amylase (fig. 8A) and TRP B289 in lipase (fig. 8C). These complementary contacts appear to govern the ligand's orientation and enhance its conformational stability. Representative 3D depictions for β-glucosidase (fig. 8D) and serine protease (fig. 8E) further illustrate how these interactions anchor ME in each enzyme's binding pocket.

Molecular docking interactions of linalool and its metabolites

Molecular docking simulations (fig. 9) demonstrated that LL and its predicted metabolites interact with α-amylase, acetylcholinesterase, lipase, β-glucosidase and serine protease through a balance of polar and nonpolar contacts. The hydroxyl moiety of LL consistently formed hydrogen bonds with residues such as ARG A52 in α-amylase (fig. 9A) and with PHE A492 and SER A452 in acetylcholinesterase (fig. 9B), while its aliphatic chain engaged in extensive hydrophobic and van der Waals interactions within the respective active-site cavities. A representative amide-containing LL metabolite exhibited a key hydrogen bond with ASP B209 in lipase (fig. 9C). For β-glucosidase and serine protease (fig. 9D and 9E), ligand stability was similarly reinforced by hydrogen bonds and the strategic accommodation of nonpolar regions into hydrophobic pockets.

Based on the provided binding affinities and reference value -4.5 ME demonstrates a more pronounced theoretical interaction with enzymes pivotal to metabolic and neurological regulation, specifically α-amylase (-5.6 kcal/mol), lipase (-5.2 kcal/mol) and acetylcholinesterase (-4.6 kcal/mol). This suggests a comparatively greater, albeit modest, potential for ME in modulating carbohydrate digestion, lipid absorption and cholinergic neurotransmission, which are therapeutic targets for diabetes, obesity and neurodegenerative disorders. Conversely, LL exhibits a slightly superior binding affinity for serine protease (-5.2 kcal/mol) and β-glucosidase (-5.4 kcal/mol). This indicates a potentially more significant role for LL in pathways related to inflammation and glycoside metabolism. While these *in silico* values denote plausible inhibitory mechanisms, they primarily serve as a rationale for prioritizing these compounds for further empirical validation through *in vitro* and *in vivo* studies to ascertain their actual therapeutic efficacy.

DISCUSSION

This study delineates the ADMET profiles and biotransformation pathways of two basil seed-derived bioactives, ME and LL, using an *in vivo* rat model. By combining UV-Vis spectrophotometry and high-resolution LC-MS/MS with in silico predictions from BioTransformer 3.0 and molecular docking, we have generated a cohesive ADMET portrait and identified key molecular interactions underpinning their bioactivity. The acute oral toxicity assessment, performed at doses up to 2000 mg/kg, demonstrated an absence of mortality or overt toxicity, underscoring a favorable safety margin for both compounds. Nevertheless, the potential implications of prolonged exposure warrant further long-term toxicological evaluation. Comparative pharmacokinetic analysis revealed that ME and LL share similar absorption kinetics-each achieving C_{max} at 4 hr (0.199 ng/mL and

0.186 ng/mL, respectively)-suggesting comparable rates and extents of initial uptake. However, their elimination profiles diverge markedly: ME exhibited a half-life of 30.0 hr and a MRT of 9.93 hr, whereas LL persisted with a half-life of 117.46 hr and an MRT of 171.05 hr. These differences reflect slower systemic clearance and prolonged exposure for LL-likely due to distinct metabolic rates, tissue distribution patterns and protein-binding interactions-and raise the possibility of accumulation under chronic dosing regimens. Collectively, these findings inform strategic chemical modifications aimed at optimizing efficacy while mitigating toxicity and lay the groundwork for subsequent functional and safety evaluations of these promising phytochemicals (Bianchini *et al.,* 2019).

The statistically significant divergence in the pharmacokinetic profiles of ME and LL is fundamentally underpinned by their distinct and well-documented metabolic fates. ME's characteristic rapid peak and sharp clearance ($p < 0.05$ at 4 hr) are attributable to its efficient biotransformation via CYP450-mediated hydroxylation, followed by swift phase II sulfation, leading to rapid elimination (Robison and Barr 2006). In stark contrast, LL, a monoterpenoid alcohol, undergoes a comparatively slower metabolic clearance, predominantly through phase II glucuronidation (Aprotosoaie *et al.,* 2014). This less expeditious conjugation pathway results in its longer elimination half-life, accounting for the significantly higher systemic concentrations observed at the 8 and 12-hr intervals ($p < 0.05$) (Bhuia *et al.,* 2025). The eventual statistical insignificance at 24 hr ($p > 0.05$) confirms that while both compounds are fully cleared, their structural differences dictate preferential and kinetically distinct enzymatic pathways, directly shaping their contrasting temporal presence in the systemic circulation.

The LC-MS/MS analysis of ME revealed a dynamic, time-dependent metabolic cascade. At 4 hr post-dose, key phase I pathways were already apparent: cyclization and demethoxylation to safrole (m/z 144.2000) and CYP1A2-mediated O-demethylation to eugenol (m/z 164). Simultaneously, CYP2C8-mediated dealkylation generated the 1,2-dimethoxybenzene fragment (m/z 137) and side-chain cleavage yielded the methoxybenzyl ion (m/z 106). These intermediate metabolites peaked between 8 and 12 hr before declining. Notably, eugenol abundance continued to rise through 24 hr, becoming the predominant species, while a secondary oxidative product-1′-hydroxymethyl eugenol (m/z 331.2000)-transiently accumulated at 8-12 hr. Collectively, these observations delineate a sequential series of oxidative, dealkylative and conjugative reactions that characterize ME's intricate *in vivo* fate.

LL underwent a similarly complex CYP450-mediated degradation pathway. Early at 4 hr, allylic hydroxylation produced 8-hydroxylinalool (m/z 142, from parent m/z 170.25) and an oxidized acyclic C_8 radical cation fragment (m/z 127), both of which diminished thereafter. Concurrent epoxidation and intramolecular cyclization yielded linalool oxide species, which were then dealkylated by CYP2C8 and CYP2C9 to form stable cyclic ether fragments (m/z 112 and m/z 102). These dealkylated metabolites maintained consistent abundance from 4 through 24 hr, indicating their relative persistence. This profile-rapid initial oxidation followed by generation of longer-lived dealkylated ethers-highlights the multi-step enzymatic degradation of LL *in vivo*.

This study demonstrates a favorable acute oral safety profile for both ME and LL, as no mortality was observed at doses up to 2000 mg/kg, implying that strategic chemical modifications of LL-like structures could further attenuate potential toxicity. However, the effects of chronic exposure remain to be elucidated. Time-resolved LC-MS/MS profiling revealed that both compounds exhibit initial chromatographic stability-ME at ~4.410 min and LL at ~0.631 min-followed by pronounced degradation by 24 hr, consistent with CYP450-mediated hydroxylation, O-demethylation and potential epoxidation, subsequent conjugative clearance and eventual epoxide ring opening. Pharmacokinetic analysis indicated that both bioactives reach their C_{max} at 4 hr post-administration (413.20 ng/mL for ME; 248.66 ng/mL for LL) and are virtually undetectable by 24 hr, reflecting rapid in vivo metabolic clearance that likely underlies their low acute toxicity.

Our molecular docking strategy targeted acetylcholinesterase-an established modulator of cholinergic neurotransmission-and key metabolic enzymes based on the documented bioactivities of basil seed constituents. This focused approach permits assessment of the neuro-modulatory potential of ME and LL metabolites, as well as their interactions with essential digestive and metabolic pathways. Such integrative investigations are critical for defining the broader physiological impacts and translational prospects of these phytochemical derivatives (Re *et al.,* 2000).

The molecular docking results indicate that ME generally achieved slightly more favorable binding energies (e.g., -5.6 vs. –5.0 kcal/mol for α-amylase), whereas LL exhibited markedly lower RMSD values-particularly against lipase (2.525-3.661 Å vs. 22.528-23.625 Å), β-glucosidase (5.747-6.125 Å vs. 19.421-21.554 Å) and serine protease (11.431-12.541 Å vs. 21.244-25.136 Å). Both compounds displayed elevated RMSD ranges when docked to α-amylase and acetylcholinesterase, suggesting conformational flexibility or multiple binding poses. ME's interactions were dominated by hydrogen bonds and hydrophobic contacts, while LL's lower RMSD values imply a more conformationally restrained, potentially more specific binding mode with certain enzymes despite its occasionally less favorable raw binding energies.

The *in silico* analysis reveals differentiated therapeutic potential, with all binding affinities surpassing the notable interaction threshold of -4.5 kcal/mol. ME demonstrates pronounced affinities for α-amylase (-5.6 kcal/mol) and lipase (-5.2 kcal/mol), suggesting a reasonable role in mitigating hyperglycemia and hyperlipidemia, cornerstone strategies in managing metabolic syndrome (Hawash *et al.,* 2021). Its binding to acetylcholinesterase (-4.6 kcal/mol) also points toward a potential, although modest, neuromodulatory capacity relevant to neurodegenerative disorders where cholinesterase inhibitors are a therapeutic mainstay (Ismail *et al.,* 2025). Conversely, LL shows superior affinity for serine protease (-5.2 kcal/mol) and β-glucosidase (-5.4 kcal/mol). This profile suggests a stronger potential in modulating inflammatory cascades, aligning with recent studies that highlight its anti-inflammatory and immunomodulatory activities (dos Santos *et al.,* 2022). While these computational findings provide a strong rationale for targeted drug discovery, they must be empirically validated to confirm their therapeutic efficacy.

Despite these promising *in silico* insights, the translational relevance of rodent-derived data must be interpreted with caution, given interspecies differences in metabolism and pharmacokinetics. Future studies should focus on the definitive structural characterization of major metabolites and on identifying the specific CYP450 isoforms responsible-ideally *via* recombinant enzyme assays or selective chemical inhibitors. Complementary *in vitro* functional assays are essential to validate the predicted ligand-enzyme interactions and a thorough investigation of phase II conjugation pathways-potentially underrepresented under the current ESI^+ conditions-will be critical to completing the ADMET profile of these bioactive phytochemicals.

Fig. 10 illustrates the putative biotransformation pathway of ME (m/z 178.10), beginning with CYP450–mediated O-demethylation and allylic hydroxylation to yield eugenol (m/z 164.08). Subsequent CYP-catalyzed dealkylation converts eugenol into 2-methoxy-4-methylphenol (m/z 138.07). Sequential demethylation and dehydroxylation steps then produce 2-methoxyphenol (m/z 124.05) and methoxybenzene (anisole; m/z 108.06), respectively. Further enzymatic cleavage culminates in benzene (m/z 78.05), which undergoes complete mineralization to CO_2 and H_2O. The empirical detection of each intermediate-validated by its characteristic m/z value in LC-MS/MS spectra-supports this degradative sequence and underscores the extensive metabolic processing of methyl eugenol *in vivo* (Chen *et al.,* 2024).

Fig. 11 depicts the proposed sequential catabolism of LL (m/z 154.14). The pathway begins with stepwise demethylation, first yielding 3-methylocta-1,6-dien-3-ol (m/z 141.12) and then 3-methylhepta-1,6-dien-3-ol (m/z 127.11). Further demethylation produces 3-methylhex-1-en-3-ol (m/z 114.10), which undergoes dealkylation to generate ethanol (m/z 46.04). Subsequent oxidation reactions convert ethanol to acetaldehyde (m/z 44.03), then to acetate (m/z 60.02) and ultimately to CO_2 and H_2O. This cascade of demethylation, dealkylation and oxidation is consistent with established terpenoid degradation mechanisms, wherein acyclic monoterpenes undergo initial functionalization followed by chain-shortening and oxidative mineralization.

The present findings lay the groundwork for a multidirectional research trajectory aimed at translating these *in silico* predictions into tangible therapeutic leads. Subsequent investigations should prioritize the empirical validation of enzymatic inhibition through quantitative *in vitro* assays and appropriate preclinical models to elucidate the precise biological mechanisms. Concurrently, comprehensive toxicological assessments are imperative to ascertain the long-term safety profiles, particularly concerning the distinct metabolic fates of each compound. Finally, these molecules serve as promising scaffolds for medicinal chemistry-driven, structure–activity relationship studies to optimize potency and pharmacokinetic characteristics, thereby guiding the rational design of novel therapeutic agents.

A key strength of this study is its combined approach, integrating live animal experiments with computational modeling. The use of high-resolution LC-MS/MS provided an accurate identification of metabolites and a notable feature of the analysis was the inclusion of RMSD values alongside binding energies, which offered deeper insight into the stability of molecular interactions. However, several limitations temper the interpretation of these findings. The results are based exclusively on male rats, which limits their generalizability, as drug metabolism often differs between species and sexes. Furthermore, the single-dose design provides no information on the potential effects of long-term exposure. Critically, the enzyme interactions predicted by computer models were not confirmed with functional lab experiments and the safety concern raised by the formation of safrole, a known toxic metabolite, was not fully addressed. While this work provides a valuable ADMET baseline, its findings should be considered preliminary until further research can establish their relevance to other models and assess long-term safety.

CONCLUSION

This study establishes that ME and LL possess low acute oral toxicity in rats (no mortality at 2000 mg/kg) and undergo rapid metabolic clearance, reaching peak serum concentrations at 4 hr and declining to negligible levels by 24 hr. Time-resolved LC-MS/MS delineated multi-step phase I pathways-hydroxylation, O-demethylation,

dealkylation and cyclization-yielding both transient and stable metabolites, while BioTransformer 3.0 predictions and molecular docking analyses provided complementary insights into CYP-mediated transformations and enzyme-ligand interactions *in silico* study delineates distinct therapeutic trajectories, identifying ME as a promising modulator of metabolic and neurological enzymes, while LL shows a preferential affinity for targets implicated in inflammatory processes. These differentiated profiles establish a compelling rationale for the targeted empirical validation required to ascertain their clinical efficacy. The empirical and *in silico* data together inform strategic structural modifications to enhance metabolic stability, minimize toxic intermediates and improve target specificity, thereby accelerating the rational design of safer, more efficacious phytochemical derivatives. Practically, the validated analytical workflows (UV-Vis and LC–MS/MS) can be adopted for high-throughput ADMET screening of related monoterpenoids and the docking results guide prioritization of lead compounds for neurological and metabolic enzyme targets. Future work should address chronic and subchronic toxicity to evaluate accumulation risks, employ recombinant CYP enzymes and selective inhibitors for definitive isoform mapping and expand LC-MS/MS methods to capture phase II conjugates.

Conflict of interest statement

The authors declare there is no conflict of interest.

Ethical approval

This was approved by the Institutional Review Board (IBR #594) of Government College University, Faisalabad, Pakistan.

Data availability

All the data is available in the manuscript.

REFERENCES

Api, AM, D Belsito, D Botelho, M Bruze, GA Burton Jr, J Buschmann, ML Dagli, M Date, W Dekant and C Deodhar (2018). RIFM fragrance ingredient safety assessment, ethyl 2-methyl-3-pentenoate, CAS Registry Number 1617-23-8. *Food Chem. Toxicol.*, **122**(Suppl 1): S612-S19.

Aprotosoaie AC, Hăncianu M, Costache II and Miron A (2014). Linalool: A review on a key odorant molecule with valuable biological properties. *Flavour Fragr. J.*, **29**(4): 193-219.

Bhuia MS, Chowdhury R, Afroz M, Akbor MS, Al Hasan MS, Ferdous J, Hasan R, de Alencar MVOB, Mubarak MS and Islam MT (2025). Therapeutic efficacy studies on the monoterpenoid hinokitiol in the treatment of Different Types of Cancer. *Chem. Biodivers*., **22**(5): e202401904.

Bianchini AE, Garlet QI, Rodrigues P, de Freitas Souza C, de Lima Silva L, dos Santos AC, Heinzmann BM and Baldisserotto B (2019). Pharmacokinetics of S-(+)-linalool in silver catfish (*Rhamdia quelen*) after immersion bath: An anesthetic for aquaculture. *Aquaculture*., 5**06**: 302-7.

Chen L, Li J, Li Q and Sun Q (2024). Hepatotoxicity induced by methyl eugenol: Insights from toxicokinetics, metabolomics and gut microbiota. *Curr. Issues Mol. Biol*., **46**(10): 11314-11325.

De Oliveira MS, Kumar R, Mali S and de Aguiar Andrade EH (2024). Methyl eugenol: Potential to inhibit oxidative stress, address related diseases and its toxicological effects. *Future Integrative Medicine*., **3**(4): 274-80.

Djoumbou-Feunang Y, Fiamoncini J, Gil-de-la-Fuente A, Greiner R, Manach C and Wishart DS (2019). BioTransformer: A comprehensive computational tool for small molecule metabolism prediction and metabolite identification. *J. Cheminform*., **11**(1): 2.

Dos Santos ÉRQ, Maia JGS, Fontes-Júnior EA and do Socorro Ferraz Maia C (2022). Linalool as a therapeutic and medicinal tool in depression treatment: A review. *Curr. Neuropharmacol*., **20**(6): 1073-1092.

El-Sonbati, AZ, NF Omar, MI Abou-Dobara, MA Diab, MA El-Mogazy, Sh M Morgan, MA Hussien and AA El-Ghettany (2021). Structural, molecular docking computational studies and *in-vitro* evidence for antibacterial activity of mixed ligand complexes. *J. Mol. Struct.*, **1239**: 130481.

Hadi NI, Jamal Q, Iqbal A, Shaikh F, Somroo S and Musharraf SG (2017). Serum metabolomic profiles for breast cancer diagnosis, grading and staging by gas chromatography-mass spectrometry. *Sci Rep*., **7**(1): 1715.

Hawash M, Jaradat N, Shekfeh S, Abualhasan M, Eid AM and Issa L (2021). Molecular docking, chemo-informatic properties, alpha-amylase and lipase inhibition studies of benzodioxol derivatives. *BMC Chem*., **15**(1): 40.

Ismail YA, Haitham Y, Walid M, Mohamed H and El-Satar YMA (2025). Efficacy of acetylcholinesterase inhibitors on reducing hippocampal atrophy rate: A systematic review and meta-analysis. *BMC Neurol*., **25**(1): 60.

Ma R, Martínez-Ramírez AS, Borders TL, Gao F and Sosa-Pineda B (2020). Metabolic and non-metabolic liver zonation is established non-synchronously and requires sinusoidal Wnts. *Elife*., **9**: e46206.

Makhdoom HS, Afzal S, Sultana K, Shah SNH, Mujahid M, Hassan ZU, Munir F, Jahan F, Abbas Z, Abid AI and Khan NUH (2024). SPE-UHPLC-ESI-MS/MS analysis of cocaine and its metabolites in conventional and alternative biological specimens: Application to real samples. *ACS Omega*., **9**(22): 23355-23363.

Munir, MU, Akash MSH and Rehman K (2025). Synthesis, characterization and biological evaluation of indole-3-

acetic acid-based hydrazone derivatives. *J. Mol. Struct.*, **1329**: 141442.

Noldner M, Germer S and Koch E (2011). Pharmacokinetics of linalool and linalyl acetate, the two main constituents of silexan, an essential oil from *Lavandula angustifolia* flowers, in rats. *Planta Medica*., **77**(12): PM44.

Re L, Barocci S, Sonnino S, Mencarelli A, Vivani C, Paolucci G, Scarpantonio A, Rinaldi L and Mosca E (2000). Linalool modifies the nicotinic receptor-ion channel kinetics at the mouse neuromuscular junction. *Pharmacol. Res*., **42**(2): 177-182.

Robison SH and Barr DB (2006). Use of biomonitoring data to evaluate methyl eugenol exposure. *Environ. Health Perspect*., **114**(11): 1797-1801.

Shah MA, Reanmongkol W, Radenahmad N, Khalil R, Ul-Haq Z and Panichayupakaranant P (2019). Anti-hyperglycemic and anti-hyperlipidemic effects of rhinacanthins-rich extract from *Rhinacanthus nasutus* leaves in nicotinamide-streptozotocin induced diabetic rats. *Biomed Pharmacother*., **113**: 108702.

Shah MA, Muhammad H, Mehmood Y, Khalil R, Ul-Haq Z and Panichayupakaranant P (2017). Superoxide scavenging and antiglycation activity of rhinacanthins-rich extract obtained from the leaves of *Rhinacanthus nasutus*. *Pharmacogn Mag*., **13**(52): 652-658.

Terfloth L, Bienfait B and Gasteiger J (2007). Ligand-based models for the isoform specificity of cytochrome P450 3A4, 2D6 and 2C9 substrates. *J. Chem. Inf. Model*., **47**(4): 1688-1701.

Wani PA, Olusesi YK, Lamiji AO, Khan MS and Chowdhury SR (2020). Bacterial biosorbents and biotransformers stimulates plant growth promotion by activation of defense mechanism and nutrient uptake. *Geomicrobiol. J*., **37**(10): 950-60.

Wishart DS, Tian S, Allen D, Oler E, Peters H, Lui VW, Gautam V, Djoumbou-Feunang Y, Greiner R and Metz TO (2022). BioTransformer 3.0-a web server for accurately predicting metabolic transformation products. *Nucleic Acids Res*., **50**(W1): W115-W123.